Enhanced phase-transfer kinetics achieved by atomic iron catalysts on hard carbon toward low-temperature sodium-ion batteries

Xinyi Qian [a], Ziling Wu [a], Jianan Gu [b], Yanli Wang [a,*], Xiaomin Cheng [c], Jing Zhang [d], Hongzhen Lin [c], Jian Wang [c,e,f,*], Liang Zhan [a,*], Yongzheng Zhang [a,*]

[a] State Key Laboratory of Green Chemical Engineering and Industrial Catalysis, State Key Laboratory of Chemical Engineering, Key Laboratory of Specially Functional Polymeric Materials and Related Technology (Ministry of Education), Shanghai Key Laboratory of Multiphase Materials Chemical Engineering, East China University of Science and Technology, Shanghai 200237, China
[b] State Key Laboratory of Alternate Electrical Power System with Renewable Energy Sources, School of New Energy, North China Electric Power University, Beijing 100096, China
[c] i-Lab & CAS Key Laboratory of Nanophotonic Materials and Device, Suzhou Institute of Nano-Tech and Nano-Bionics, Chinese Academy of Sciences, Suzhou 215123, China
[d] School of Materials Science and Engineering, Xi'an University of Technology, Xi'an 710048, China
[e] Helmholtz Institute Ulm (HIU), Ulm D89081, Germany
[f] Karlsruhe Institute of Technology (KIT), Karlsruhe D76021, Germany

Keywords:
Sodium ion battery
Single atom catalyst
Phase transfer kinetics
Hard carbon
Low temperature

A B S T R A C T

Hard carbons with desirable pore morphologies are the most promising anode materials for sodium-ion batteries, but experience undesirable cycling stability and depressed capacity owing to sluggish reaction kinetics of sodium-related species through or across the carbon layer. Herein, based on closed pore morphology engineering using carbon dioxide physical activation method, the hard carbon composite (SAFe@HC) was prepared by coating a polydopamine capping layer with uniformly distributed iron single atoms on the closed-pore-rich hard carbon, where the introduction SAFe help to expand the layer spacing distance, providing additional channels for solvated Na^+ diffusion. It is innovatively proposed that SAFe catalysts provide abundant active catalytic sites for accelerating the interfacial desolvation and the phase-transfer kinetics of Na^+ is lowered by decreasing the sodium ion transport energy barrier, as confirmed by theoretical simulation and various electrochemical demonstration. In addition, the closed pore morphology also enhances the surface area and adsorbs more sodium ions. As a result, the SAFe@HC electrode exhibits a high reversible capacity of 340.7 mAh g^{-1} and a remarkable rate capacity up to 306.2 mAh g^{-1} and a high capacity-retention of 96.0% after 500 cycles at 5 C. Decreasing the environmental temperature to 0 °C, an excellent robust electrochemical performance of 172.2 mAh g^{-1} at 5 C, offering promising avenues of single atomic catalysts achieving high-rate hard carbon electrode for sodium-ion batteries.

1. Introduction

Thanks to the abundance of sodium resources and fast-charging capability, sodium-ion batteries (SIBs) represent a low-cost alternative to lithium-ion batteries, which will be extensively employed in large-scale energy storage and low-speed electric vehicles [1–4]. Among the numerous anode materials, carbon-based material is widely regarded as the highly promising one due to its advantages of wide range of sources, unique structural stability and low cost. Among the various carbon-based materials that have been identified as potentially suitable, biomass-derived hard carbon is regarded as one of the most promising candidates [5–8]. The rich closed-pore structure and morphology in biomass-derived hard carbon give it an excellent platform capacity with a low voltage plateau [9]. However, the large ionic radius of Na^+ and

* Corresponding authors at: i-Lab & CAS Key Laboratory of Nanophotonic Materials and Device, Suzhou Institute of Nano-Tech and Nano-Bionics, Chinese Academy of Sciences, Suzhou 215123, China; Helmholtz Institute Ulm (HIU), Ulm D89081, Germany; Karlsruhe Institute of Technology (KIT), Karlsruhe D76021, Germany (J. Wang).
E-mail addresses: ylwang@ecust.edu.cn (Y. Wang), jian.wang@kit.edu, wangjian2014@sinano.ac.cn (J. Wang), zhanliang@ecust.edu.cn (L. Zhan), zhangyongzheng@ecust.edu.cn (Y. Zhang).

Na^+ solvation shell inevitably lead to the bottleneck of sluggish sodium diffusion kinetics and suboptimal cycling stability [10].

Generally, hard carbon is achieved after high-temperature carbonization, where the sp^3 hybridization takes place during the early stages of carbonization to form a three-dimensional crosslinked structure, hindering the growth of the carbon layer. Additionally, small molecules such as H_2O, CO_2, CO help to generate randomly orientated microstructure with highly developed porosity, guaranteeing disordered graphene nanosheets with abundant pores and defect turbine structures [11]. As known, the sodium behaviors on hard carbon anode are divided into a sloping region and a plateau region, corresponding to sodium adsorption on the carbon surface, intercalation between carbon layers and the formation of quasi-metallic Na clusters in the pores, respectively [12]. The layer spacing (d_{002}) of hard carbon of 0.37 nm is considered to be the smallest d_{002} for sodium embedding and diffusion. In recent years, attempts have been made to optimize the layer spacing to obtain electrochemical properties of hard carbon [13–15], enriching the closed pore structures [16], and modulating the surface defects of hard carbon [17]. However, the layer spacing expansion is limited and it might fail to help to transport large $Na(solvents)_x^+$ species, inducing worse performance under low-temperature environmental surroundings.

Alternatively, isolated metal single atoms have well-defined activity centers and ideal atom utilization of 100% [18–24]. Increasing attentions have been paid of adopting the single atomic catalysis strategy in hard carbon anodes. Numerous studies have shown that single-atom doping can alter the electronic structure of the active site, enhancing the affinity of the Na ions and generating delocalized electrons to achieve more catalytic sites [25–31]. For example, metal single atoms into hard carbon elucidated that the single metal atoms could construct a fast charge conduction network and help to form an inorganic-dominated SEI layer, thereby promoting sodium ion migration kinetics [32–36]. As discussed above, before sodiathiation reaction, the sodium species should be partially or completed dissociated, contributing much higher energy barriers. However, little attention focuses on the desolvation process and the related Na^+ transfer across the pore layer.

Herein, based on the pore morphology engineering, an atomic metal catalyst of iron has been proposed on hard carbon (SAFe@HC) to accelerate the desolvation and diffusion kinetics. The heteroatom decoration also enhances the layer spacing distance of d_{002}, which helps to propel Na^+ diffusion in the interior and across the interface. Meanwhile, the SAFe provide abundant active catalytic sites for accelerating the interfacial desolvation and the phase-transfer kinetics of Na^+ is lowered by decreasing the sodium ion transport energy barrier, as confirmed by theoretical simulation and various electrochemical demonstration. In addition, the closed pore morphology also enhances the surface area and adsorb more sodium ions. Compared to the HC, the SAFe@HC displays excellent sodium storage performance with a charge specific capacity of 340.7 mAh g^{-1} at 0.1 C and a capacity retention of 96.0% after 500 cycles at 5 C. In addition, the reversible charging specific capacity of SAFe@HC electrodes was found to be 172.2 mAh g^{-1} at a low temperature (0 °C), with a capacity retention rate of 80.5% observed after 250 cycles. This work demonstrates the single atomic catalysts induce surface electron redistribution, catalyze the dissociation of solvated structures for fast-charging low-temperature sodium batteries.

2. Experimental section

2.1. Materials

Pluronic F-127 ($H(C_2H_4O)_x(C_3H_6O)_y(C_2H_4O)_zOH$, ≥99%, AR), dopamine (DA, ≥98%, CP), ammonia solution (25–28%, CP), and Iron (III) nitrate nonahydrate (≥99%, AR) were obtained from Macklin. All the chemical reagents were used as received and without further purification. GF/D separator, Super C, Cu foil, electrolyte, polyvinylidene difluoride (PVDF), 1-Methyl-2-pyrrolidinone (NMP) were bought from Guangdong Canrd New Energy Technology Co., Ltd.

2.2. Synthesis of hard carbon

The raw coconut shell charcoal was subjected to ball milling at 300 rpm for 4 h, with the objective of obtaining a coconut shell charcoal powder characterized by a uniform particle size distribution. The coconut shell carbon was placed within a quartz tube and subjected to a physical activation process at 700 °C for 2 h. This process was conducted under a carbon dioxide atmosphere, resulting in the formation of a porous coconut shell carbon material. Subsequently, the porous carbon was held at 1400 °C for 2 h and then cooled naturally in an argon-filled tube furnace. This process resulted in the formation of coconut shell carbon with a high concentration of closed pores, designated as YK-1400.

2.3. Synthesis of SAFe@HC and HC

40 mL Pluronic F-127 dissolved in ethanol (20 mg mL^{-1}), 400 mg dopamine and 0.4 mmol ferric nitrate were added sequentially to a 40 mL YK-1400 aqueous suspension and stirred until the material was homogeneously dispersed. A solution of 1 mL ammonia (25–28%) was added and the mixture was stirred for 12 h at room temperature. Subsequently, centrifugation was performed to obtain the iron-coordinated PDA-coated hard carbon, which was then washed three times with deionized water and dried under vacuum. The dried powder was heated to 800 °C in an argon atmosphere at a heating rate of 5 °C min^{-1}, and then annealed at this temperature for 3 h. Ultimately, the product was introduced to a 2 M hydrochloric acid solution, where it underwent a 12-hour reaction to yield SAFe@HC

The identical experimental procedure was employed in the absence of iron nitrate in order to obtain the comparison sample, named HC. Furthermore, the comparison sample (SAFe@C) was generated by omitting the high-temperature treatment of 1400 °C throughout the experimental process.

2.4. Assembly of cells

The weight ratio of the active material, conductive carbon Super C, and the polyvinylidene fluoride was 7:2:1. Subsequently, an appropriate quantity of NMP was added to create a slurry. The electrode slurry was deposited onto the carbon-coated copper foil. The coated copper foil was subjected to a drying process in a vacuum oven at a temperature of 80 °C for a period of 12 h. Following this, the electrodes were punched into circular sheets with a diameter of 12 mm. The mass loading of the active material of SAFe@HC is approximately 1.3 mg cm^{-2}.

3. Result and discussion

3.1. Structural characterization

Fig. 1a illustrates the synthesis of SAFe@HC. In brief, the present strategy employs an oxidative self-polymerization reaction to generate a dopamine coating layer on hard carbon with monodisperse Fe metal ions. The hard carbon utilized in this study was initially subjected to a physical activation process with CO_2 to enrich the pore structure of the coconut shell carbon, as shown in Fig. S1a and b. It is noteworthy that the Fe ions at elevated temperatures (>900 °C) can result in the aggregation of Fe nanoparticles (Fe NPs), thereby creating potential issues during the synthesis process. To circumvent this challenge, the synthesis pathway was designed to commence with the high-temperature carbonization of coconut shell charcoal, followed by the application of polydopamine coating [37]. The dopamine molecule is characterized by high-content catechol (–OH) and amino ($–NH_2$) functional groups, which undergoes an oxidative self-polymerization reaction in alkaline conditions, forming polydopamine (PDA) coatings on a diverse range of

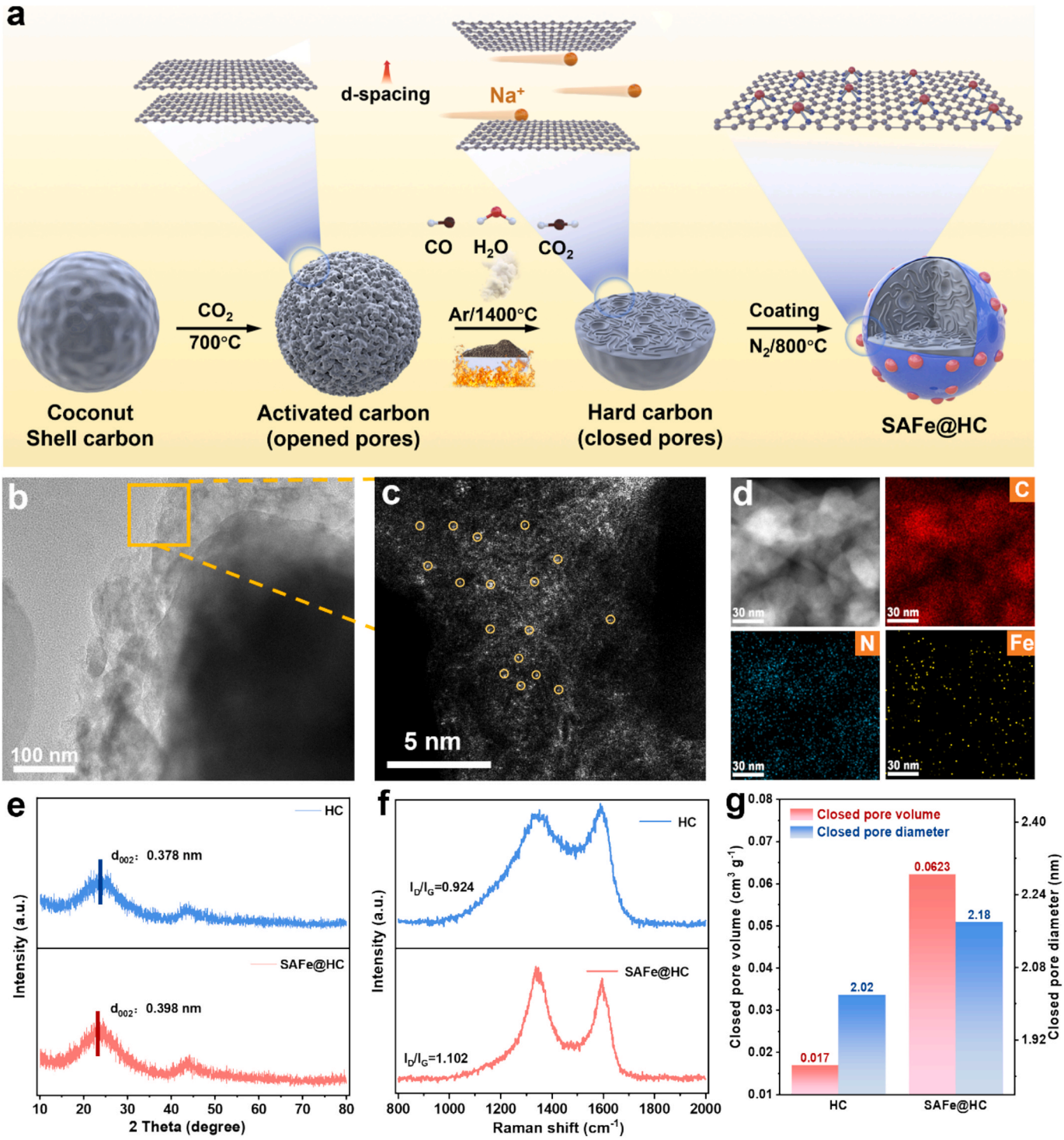

Fig. 1. Synthesis and characterization of the SAFe@HC and HC. a) Schematic illustration of the synthesis procedure for SAFe@HC; b) TEM image, c) aberration-corrected HAADF-STEM image (Fe-single atoms highlighted by yellow circles) and d) EDS elemental mapping of SAFe@HC; e) XRD patterns, f) Raman spectra, g) closed pore diameter and closed pore volume of SAFe@HC and HC. (For interpretation of the references to colour in this figure legend, the reader is referred to the web version of this article.)

substrates. Moreover, the abundant N-containing sites can coordinate with SAFe to prevent the agglomeration. As illustrated in Fig. 1b, transmission electron microscopy (TEM) image shows that the SAFe@HC has a uniform cladding layer that provides an artificial solid-electrolyte interphase film for the internal hard carbon [38,39]. Moreover, the high-temperature calcination process (>1000 °C) of the hard carbon precursor is accompanied by the growth of graphene layers and the transition from open to closed pores. The high-resolution TEM image (Fig. S1c) reveals the presence of a large number of closed pores, which are surrounded by random and tightly stacked carbon layers. An elemental iron content of 0.15 wt% was ascertained by means of inductively coupled plasma mass spectrometry (ICP-MS) analysis. In order to further examine the presence form and dispersion of iron, an aberration-corrected high-angle annular dark-field scanning transmission electron microscope (HAADF-STEM) was used. As illustrated in Fig. 1c, the HAADF-STEM images show the presence of many bright

spots delineated by yellow circles on the SAFe@HC cladding layer, indicating that the iron elements are uniformly distributed in the form of atoms on SAFe@HC [40]. The uniform distribution of C, N, and Fe elements on the hard carbon matrix is observed in the energy dispersive X-ray spectrogram (EDS) in Fig. 1d, thereby providing further visual evidence of a homogeneous distribution of iron monoatoms.

As shown in Fig. 1e and f, Raman spectra and X-ray diffraction (XRD) demonstrate that SAFe@HC has higher disorder degree and larger layer spacing, proving that the SAFe introduce more active sites into the material. The layer spacing (d_{002}) of SAFe@HC can be calculated as 0.398 nm by Bragg equation, which is a favourable value for Na^+ embedding [41–43]. Concurrently, the same layer spacing can be calculated by the speckle stripes in TEM (Fig. S1c), corroborating with the XRD results. The widening of the d_{002} due to the Fe-C bonds on the surface of the material inducing a redistribution of the electron density on the hard carbon, and may reduce the diffusion energy barrier for sodium ions in the bulk phase. In addition, the XRD spectra did not show specific peaks associated with iron and their compounds, further proving the presence of SAFe.

To gain further insight into the structural characteristics of the closed pores, a detailed analysis using Brunauer-Emmett-Teller (BET) and small-angle X-ray scattering were conducted. As illustrated in Fig. S2, the BET results showed that the open pores were effectively inhibited by the polydopamine coating and that the samples containing single atoms introduce more defects into the material. Additionally, both SAFe@HC and HC exhibit distinctive scattering intensity within the range of 0.1–0.2 Å in SAXS results, substantiating the presence of copious nanoporous structures [44]. A detailed analysis of the scattering intensity profiles indicates that the HC sample exhibits a pronounced oscillation in the tail, which may be attributed to the reduction in the scattering signal resulting from the less developed pore structure. After Porod correction of the data, the Stevens & Dahn algorithm was used to fit the curves (Fig. S3a) and combined with the pore data from BET to obtain detailed information on the nano-closed pore structure (Table S1). As evidenced in the literature [45], the dimensions of sodium clusters are approximately 1.3–1.5 nm. Consequently, a pore size that is too narrow will impede the ingress of sodium clusters into the closed pore. As illustrated in Fig. 1g, the mean diameter of the closed pore of SAFe@HC is notably larger (2.18 nm), and the closed pore volume is also considerably larger (0.0623 cm^3 g^{-1}), respectively. This pore structure is more conducive to the embedding of sodium clusters. Therefore, it can be demonstrated that the secondary carbonization process to introduce Fe single atoms provides a denser distribution of closed pores for the hard carbon. Further detailed information regarding the size distribution of pores can be found in Fig. S3b and c.

3.2. *Contribution of closed pores in sodium storage performance*

The electrochemical performance of the samples was investigated by Na||HC half-cells assembled with ester-based electrolyte [46]. Initially,

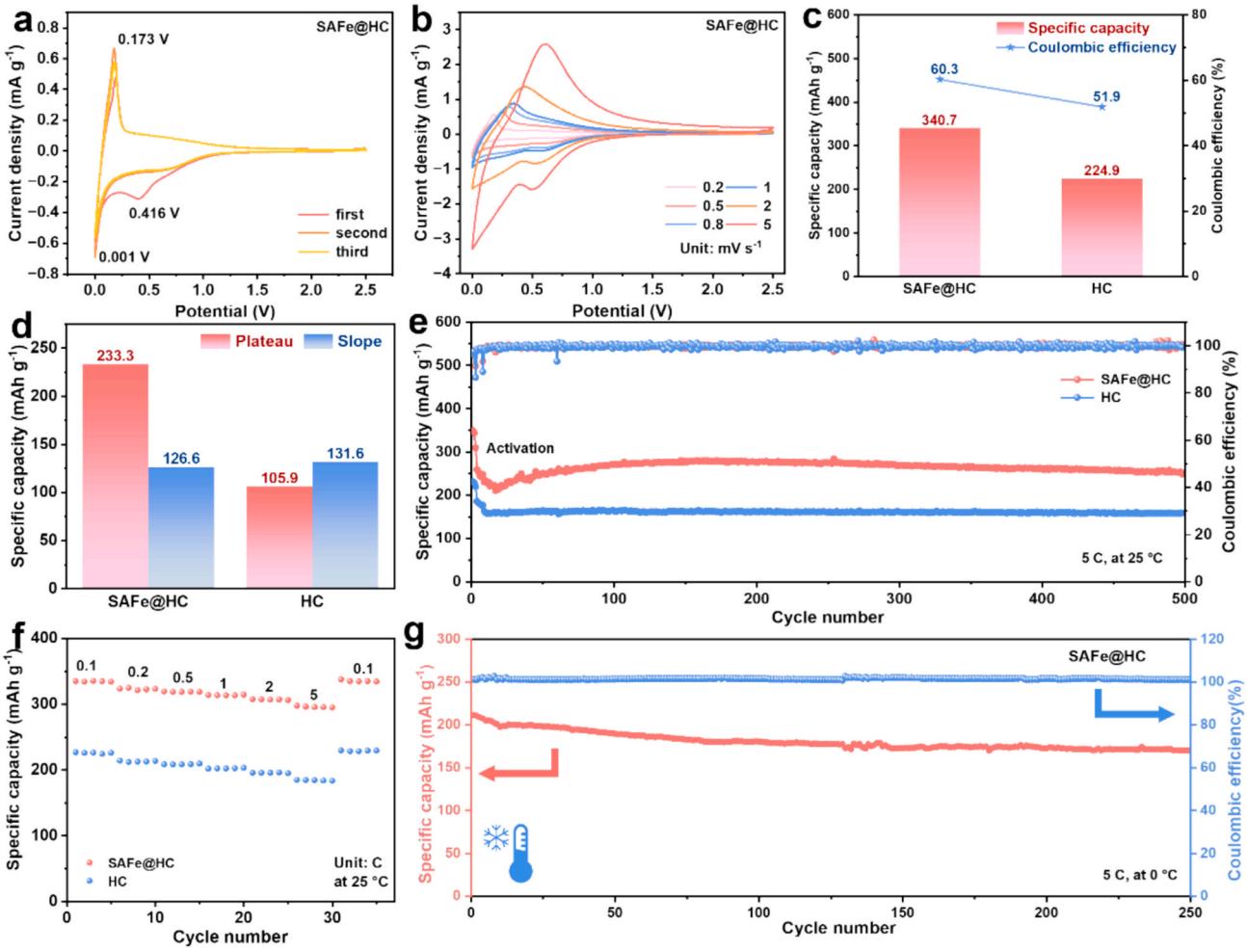

Fig. 2. Electrochemical measurements. a) CV curves of SAFe@HC anode at 0.2 mV s^{-1}; b) CV curves of SAFe@HC anode at scan rate from 0.2 to 5.0 mV s^{-1}; c) Charge capacity at 1st cycle and initial Coulombic efficiency of different hard carbon anodes; d) Comparison of the plateau and sloping capacity based on the 2nd discharge/charge curves; e) Cycling performance at 5 C at 25 °C; f) Rate capability of SAFe@HC and HC anode; g) Cycling performance of SAFe@HC anode at 0 °C.

cyclic voltammetry (CV) measurements were conducted to examine the electrochemical behavior of the prepared samples. As shown in Fig. 2a, the reduction peak at 0.416 V is exclusive to the first circle, indicating that it correlates with the formation of a SEI layer and other irreversible reactions that deplete the electrolyte. The reduction peak at 0.617 V corresponds to the redox reaction between Na^+ and C═O groups, while the peak at 0.001 V corresponds to the filling of sodium metal clusters at the plateau region. The SAFe@HC electrode delivered the sharpest redox peaks due to the proximity of its active substance clusters, indicating an ultrafast Na^+ diffusion reaction kinetics. To further elucidate the mechanism and kinetics of sodium storage in SAFe@HC, CV test was further conducted at various scanning rates. As illustrated in Fig. 2b and Fig. S4a, the CV curves of the SAFe@HC electrode exhibit comparable peak profiles as the scan rate increased, and the redox peaks retain a robust current response, demonstrating the SAFe@HC possesses an exceptional capacity at elevated current densities. In contrast, the feeble current response of SAFe@C (Fig. S4c) suggests that the capacity is predominantly attributable to the abundant closed pores and expanded d-spacing. Consequently, modulating the closed pore structure of hard carbon materials can markedly enhance their sodium storage performance.

In order to further elucidate the correlation between closed pore structure and sodium storage capacity, a series of galvanostatic charge/discharge (GCD) tests were performed. As illustrated in Fig. S4d, the GCD curves of SAFe@HC and HC anodes can be divided into two distinct regions: the slopping region (>0.1 V) and the plateau region (<0.1 V). The unmodified coconut shell hard carbon displays a smaller plateau region in the GCD curve, a consequence of the 0.378 nm layer spacing. In addition, the SAFe@HC and HC electrodes show the clear voltage plateau around 0.6 V, which can be attributed to the redox reaction between Na^+ and C=O groups [47]. X-ray photoelectron spectroscopy (XPS) results (Fig. S6) indicate that the intensity of the C=O peak (289 eV) of SAFe@C is relatively weak, which is consistent with the absence of voltage plateau near 0.5 V in the GCD curve [48]. The initial discharge capacities of SAFe@HC and HC anodes were found to be 565.3 and 433.6 mAh g^{-1} at 0.1 C. Fig. 2c illustrates the reversible charge capacity at the 1st cycle and ICE of SAFe@HC, which are 340.7 mAh g^{-1} and 60.3%, respectively. These values are significantly higher than those of HC (224.9 mAh g^{-1}, 51.9%). In addition, by analysing the percentage of the plateau capacity of SAFe@HC during the second cycle of discharge, finding that the plateau capacity of the sample accounted for 64.8% of the total capacity, with a value of 233.3 mAh g^{-1} (Fig. 2d). In comparison, a lower percentage of platform capacities are observed in HC electrode (105.9 mAh g^{-1}, 44.6%). In light of the findings from the preceding section regarding the SAXS calculations, it can be posited that the diameter and volume of closed pore are significant factors influencing the sodium storage properties of hard carbon anode.

3.3. Contribution of SAFe in sodium storage performance

The capacity of cycling and rate were conducted on SAFe@HC and HC electrodes (Fig. 2e and f), where the SAFe@HC anode demonstrated higher reversible capacity at all current rates, and eventually recovered to 334.6 mAh g^{-1} without capacity attenuation, suggesting an excellent rate performance and rapid Na^+ reaction kinetics by SAFe@HC. Even at a high current rate of 5 C, the reversible capacity of SAFe@HC anode is constrained to 295.1 mAh g^{-1}, superior to that of HC anode (183.7 mAh g^{-1}). Besides, the SAFe@HC anode also demonstrates an outstanding long-cycle performance after 500 cycles at 5 C with a capacity of 249.1 mAh g^{-1} and a capacity retention rate of up to 96.0%. In contrast, the HC anode did not exhibit a decreasing and then increasing trend in long cycling, which might be caused by the lack of catalysis by single atoms, and its specific capacity was only 159 mAh g^{-1} after 500 cycles. Moreover, the cycling stability of the SAFe@HC anode was evaluated under low-temperature condition (0 °C) (Fig. 2g). The cells were fully activated at 0.1 C and subsequently subjected to a cycling regimen at 5 C for 250 cycles. Impressively, the low-temperature capacity was found to be only 18.5% lower than that of the ambient temperature, with a capacity retention of 80.5%.

In order to gain insight into the sodium storage behavior and reaction kinetics of hard carbon anodes, an in-depth analysis of the CV curves was conducted using a range of scan rates [49,50]. The relationship ($i = a\,v^b$) between the peak redox current (i) and the scan rate (v) allows the calculation of the b value. The b value is a key parameter for the evaluation of whether the process is diffusion-controlled (when the b value is close to 0.5) or surface-induced capacitive controlled (when the b value is close to 1). As shown in Fig. 3a and Fig. S5, the oxidation/reduction peak currents of CV curves were selected at each scan rate to obtain the slope of the fitted line. The b values of SAFe@HC anode were 0.76 and 0.64, respectively, which were higher than HC anode (0.68, 0.51), indicating that the conversion kinetics of SAFe@HC is governed by the surface capacitance in conjunction with the ion diffusion behavior. The samples with SAFe displayed higher b-values upon comparison, indicating that SAFe facilitates accelerated reaction kinetics. The total capacity can be divided into diffusive and pseudocapacitive contributions on the basis of the sodium ion storage mechanism. The sloping capacity region and the low-voltage plateau region are controlled by surface capacitive behavior and diffusive behavior, respectively. Furthermore, the capacitance capacity can be calculated using the following equation: $i/v^{1/2} = k_1v + k_2v^{1/2}$. As illustrated in Fig. 3b and Fig. S7, the pseudocapacitance contribution demonstrates an increase in accordance with an increase in scanning rate. At a scan rate of 1 mV s^{-1}, the capacitance contribution of SAFe@HC is found to account for 55.8% of the total capacitance, indicating that the rich catalytic sites from SAFe and closed pores provide effective physicochemical adsorption. In order to more effectively assess the optimization of Na^+ adsorption by Fe single atoms, DFT calculations were employed to ascertain the adsorption energy of SAFe@HC and HC with Na^+ (Fig. 3c). It is notable that the adsorption energy of sodium ions on HC is 0.38 eV, which is lower than that observed for SAFe@HC (1.25 eV). These findings suggest that SAFe@HC may provide a greater number of active sites and ultimately attain more Na^+ in the adsorption phase of sodium storage. Additionally, the disparate charge densities ($\Delta\rho$) of HC and SAFe@HC (Fig. S8) suggest SAFe facilitates the transfer of electrons to neighboring nitrogen atoms, thereby forming negatively charged core and achieving a high sodium storage capacity at the single atomic site [51]. The electrode materials were subjected to analysis via the galvanostatic intermittent titration technique (GITT) at 0.1 C, with the objective of elucidating the impact of iron monoatomic doping on the diffusion process. The diffusion coefficients (D_{Na}^+) during sodiation/desodiation were calculated in accordance with the equation $D = \frac{4}{\pi\tau}\left(\frac{n_m v_m}{s}\right)^2\left(\frac{\Delta E_s}{\Delta E_t}\right)^2$. As shown in Fig. S9, the diffusion coefficients of the SAFe@HC electrodes exhibited heightened and more consistent values throughout the entirety of the charging and discharging processes, demonstrating the monoatomic facilitation of sodium ions across closed-pore interfaces. It is noteworthy that during the discharge process, the diffusion rate experiences a sharp decline at approximately 0.1 V, followed by a rapid recovery. This decline corresponds to the embedding of sodium ions through the carbon layer into the closed pores, while the rebound phase is associated with the rapid diffusion kinetic of Na^+ ions into the nanopore and subsequent filling of the nanopore [52].

To gain further insight into the Na^+ storage kinetics of SAFe@HC anode during the charging and discharging process, the diffusion and desolvation barrier energy of Na^+ in both models was calculated using DFT theory, according to the selected diffusion paths. As illustrated in Fig. 3d, the diffusion energy barrier of SAFe@HC is lower than that of HC, indicating that it is more conducive to Na^+ diffusion, in agreement with the diffusion coefficient results obtained by GITT. This phenomenon may be attributed to the sodalophilicity of the SAFe and its induced formation of large interlayer spacing. The extended layer spacing

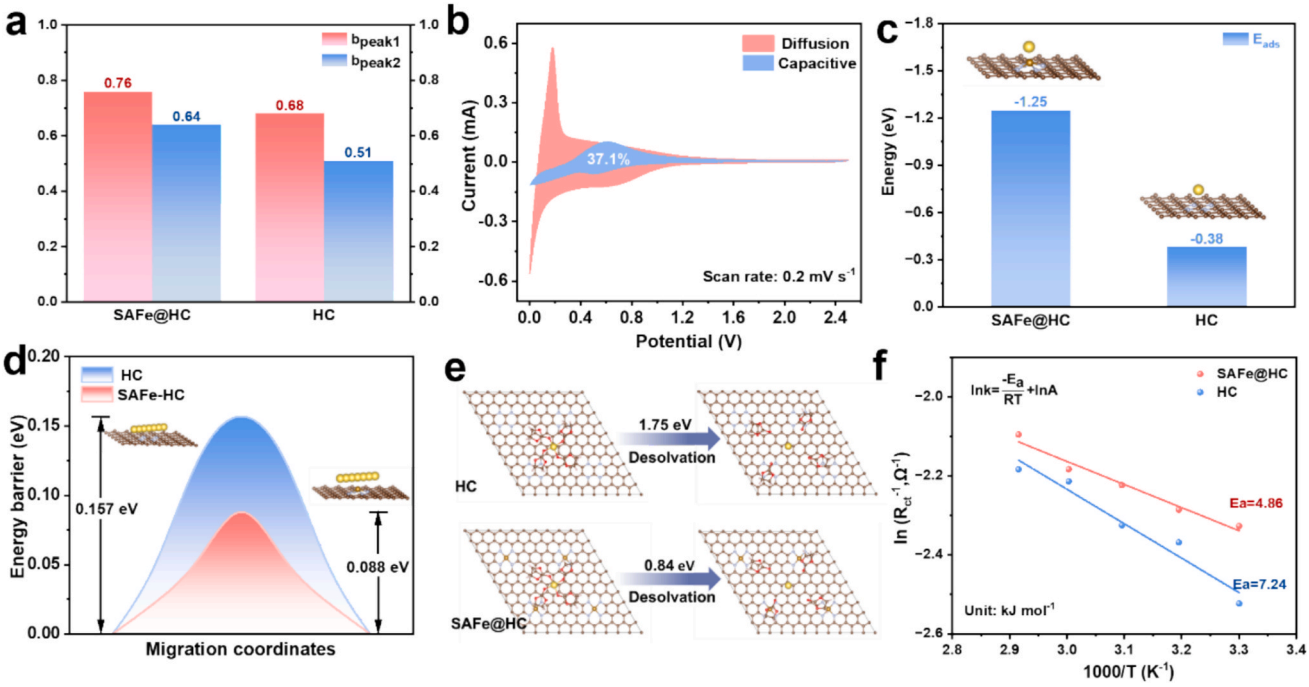

Fig. 3. Phase interface diffusion of Na^+. a) The determined *b* values calculated through the liner relationship of the redox peaks; b) The capacitive-controlled CV curve at 0.2 mV s^{-1} of SAFe@HC electrode; c) DFT calculations of adsorption energies; d) Diffusion barrier energies of Na^+; e) Desolvation barrier energies of HC and SAFe@HC; f) Arrhenius curves and the calculated activation energies as obtained from the Nyquist plots.

(elevated from 0.378 nm to 0.398 nm) directly reduces the diffusion energy barrier of sodium ions in the bulk phase. At the same time, the highly active sites provided by the single atoms preferentially adsorb Na^+ from the electrolyte, accelerating the migration of Na^+ into the bulk phase. Typically, the desolvation is the slowest kinetic step in electrochemical processes [53–58]. As shown in Fig. 3e, the SAFe@HC has a much lower energy barrier for desolvation, implying that the SAFe can act as a pre-desolvation catalyst to promote the desolvation of Na ions on the SEI layer [33,59,60]. In conclusion, the modulation of hard carbon by iron single atoms may provide a multitude of catalytic sites on the surface and generate a localized electric field, facilitating rapid charge transfer and desolvation kinetics.

It is well established that hard carbon anodes possess a stable structure, with their cycling stability largely contingent upon the stability of the SEI layer. Electrochemical impedance spectroscopy (EIS) was conducted on the SAFe@HC and HC anodes prior to and following the cycling process. The EIS results (Fig. S10) revealed that the charge transfer impedance of the SAFe@HC electrode was lower than HC both before and after 200 cycles. In addition, the sample containing SAFe exhibited lower impedance and higher diffusive electron conductivity after cycling, suggesting that the SAFe provide a low-impedance charge transport channel, which is consistent with the GITT results. To gain further insight into the interfacial charge transfer kinetics of SAFe@HC, EIS were conducted on the electrodes at varying temperatures. The activation energy of the charge transfer process for the electrodes was subsequently calculated using the Arrhenius equation (Fig. 3f) [61]. The activation energies of SAFe@HC and HC anodes were found to be 4.86 and 7.24 kJ mol^{-1}, respectively, suggesting that the doped SAFe play a role in reducing the desolvation energy barrier, thus facilitating the diffusion and storage of Na ions.

Fig. 4a and Fig. S11 illustrate the TEM images of SAFe@HC, and HC electrodes following 300 cycles [62–64]. The surface of SAFe@HC exhibits a SEI layer with a uniform thickness of 4 nm, which is less than that observed for HC (14 nm) electrode. The formation of a thinner and more homogeneous SEI layer facilitates enhanced Na^+ transport kinetics and improved initial Coulombic efficiency. As illustrated in Fig. 4a, the surface of the SAFe@HC electrode exhibits a SEI layer comprising an amorphous outer layer and a crystalline inorganic inner layer. The nanocrystal exhibits a lattice stripe spacing of 0.24 nm, corresponding to the (200) face of the NaF, that may correspond to the dissociation of PF_6. It is worth noting that the inorganic components have lower Na^+ diffusion activation energies (100–150 meV) and electronic insulating properties than organic substances, so the NaF-rich SEI layer with strong mechanical strength can effectively prevent further decomposition of the electrolyte and promote interfacial Na^+ storage kinetics [46,47]. In order to investigate the component composition of the SEI layer, the three electrodes after 10 cycles were subjected to deep etching XPS spectroscopy of F 1s (Fig. 4b). It is notable that the proportions of Na-F peaks in the samples with SAFe@HC anode are markedly higher than that in the HC anode. This result indicates that the SAFe exert an important role in modulating the composition of the SEI layer, thereby promoting the formation of a NaF-rich SEI layer. Furthermore, a notable distinction exists in the composition between the surface layer and the inner layer of the electrode sheet. As shown in Fig. 4c, all three electrodes demonstrate a pattern of continuous enhancement of the Na-F peak as the etching depth increasing, with the fastest growth rate observed for SAFe@HC anode.

To gain further insight into the chemical composition of the SEI layer, time-of-flight secondary ion mass spectrometry (TOF-SIMS) was employed. The 3D TOF-SIMS maps (Fig. 4d) provide a visual evidence of the chemical composition and distribution of the SEI layer in different anodes [65–67]. As reported, the homogeneous dispersion of Na and F^2 derived chain segments reflects the enrichment of inorganic compounds (NaF) in the SEI layer [68]. A combination of the depth distribution plots of the sputtered volume of the SEI layer (Fig. 4e and Fig. S12) and the in-depth XPS elemental atomic content variation plots (Fig. 4f) reveal that the Na elemental content increases and the F elemental content decreases with the increasing depth. This phenomenon correlates with the generation of the inorganic component NaF within the inner layers of the SEI, as well as the storage of metallic sodium clusters. Furthermore, a greater proportion of F^2 species was identified in the SEI layer of SAFe@HC in comparison to samples

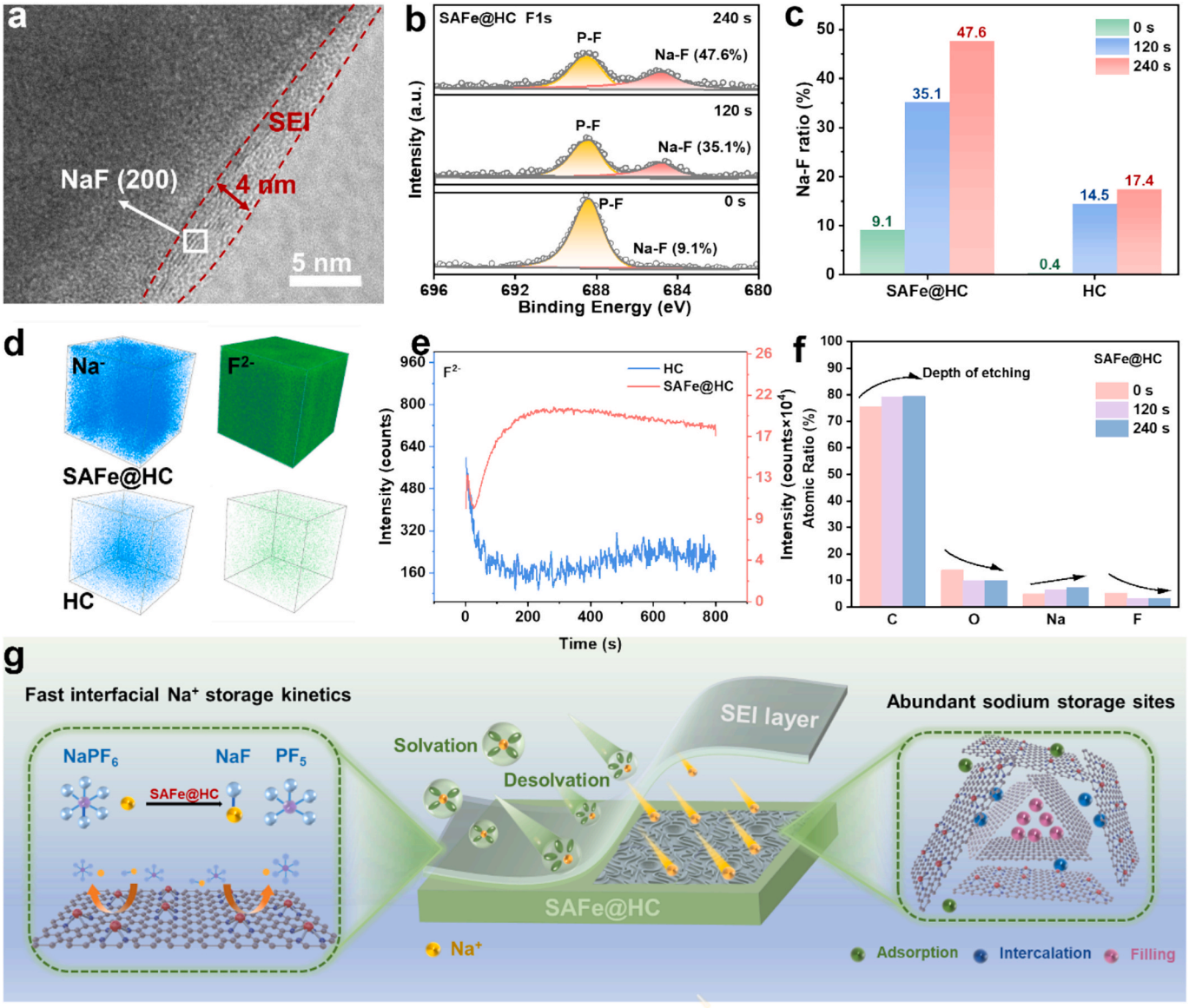

Fig. 4. Influence of single atoms on the SEI layer and sodium storage mechanism. a) HRTEM image of cycled SAFe@HC electrode (5 C, 300th cycle, 25 °C); b) In-depth F 1s XPS spectra of the SEI with different Ar^+ sputtering time; c) Comparison of Na-F ratio in different anodes; d) TOF-SIMS visual maps in the SEI of SAFe@HC and HC anodes; e) Depth profiles of F^{2-} species contained in the sputtered volume at the SEI layer; f) Atomic percentages of C, O, Na and F by in-depth XPS after 10th cycle; g) The schematic diagram of the Na^+ storage mechanism in SAFe@HC anode.

without SAFe, indicating that the incorporation of the SAFe facilitates the induction of the fluorine component. These results of in-depth and TOF-SIMS analysis both demonstrated that the incorporation of iron monoatoms regulates the composition of the SEI film, thereby influencing the fluorine component of the electrolyte and resulting in the formation of a thin and robust SEI layer.

As shown in Fig. 4g, combining the experimental results and DFT analyses, a possible mechanism to enhance the sodium storage performance of SAFe@HC anode is proposed. The sodium storage mechanism of hard carbon materials can be typically divided into three steps: adsorption, intercalation and filling. Firstly, the formation of negative charge centres induced by SAFe can act as a pre-dissolution, which promotes the dissociation of solvent molecules from the Na^+-solvated sheaths, releasing more bare Na^+ and accelerating the ion diffusion kinetics at the electrode/electrolyte interface. In the adsorption phase, SAFe provide abundant active sites with reduced adsorption energy for sodium storage. In the intercalation stage, the enlarged layer spacing and abundant closed-pore configurations then provide favourable conditions for sodium metal filling. Finally, in the filling stage, sodium ions form quasi-sodium metal clusters at low voltage, and the catalytic role of iron monoatoms lowers the barriers for sodium ions to cross the phase interface, resulting in a sharp increase in the diffusion coefficient and providing the basis for excellent low-temperature performance. In addition, the catalytic sites provided by SAFe reduce the dissociation energy for P-F bond breaking, resulting in the formation of an inorganic (NaF)-dominated SEI layer. The NaF-rich SEI layer reduces the Na^+ diffusion activation energy and provides a channel for rapid charge transfer.

4. Conclusion

In summary, to accelerate the desolvation process and related Na^+ transfer across the pore layer and the dissociation of $Na(solvents)_x^+$ species, the single atom catalyst strategy has been proposed to accelerate the related kinetics based on pore structure with abundant closed pores of hard carbon. The introduction of SAFe helps to expand the layer

spacing distance, providing additional channels for solvated Na^+ diffusion and ion phase transfer, as confirmed by theoretical simulation and various electrochemical demonstration. A remarkable rate capacity up to 306.2 mAh g^{-1} and high capacity-retention of 96.0% after 500 cycles at 5 C is achieved. Decreasing the environmental temperature to 0 °C, an excellent robust electrochemical performance of 172.2 mAh g^{-1} at 5 C is obtained, providing a feasible strategy to enhance the Na^+ phase transfer kinetics through the electron redistribution function of the single-atom catalyst for sodium-ion batteries.

CRediT authorship contribution statement

Xinyi Qian: Writing – original draft, Visualization, Methodology, Investigation, Formal analysis, Data curation, Conceptualization. **Ziling Wu:** Visualization, Data curation. **Jianan Gu:** Visualization, Conceptualization. **Yanli Wang:** Visualization, Conceptualization. **Xiaomin Cheng:** Validation, Formal analysis. **Jing Zhang:** Validation, Conceptualization. **Hongzhen Lin:** Visualization, Conceptualization. **Jian Wang:** Writing – review & editing, Methodology, Investigation. **Liang Zhan:** Methodology, Funding acquisition. **Yongzheng Zhang:** Writing – review & editing, Investigation.

Declaration of competing interest

The authors declare that they have no known competing financial interests or personal relationships that could have appeared to influence the work reported in this paper.

Acknowledgements

This work is supported by the funding from the National Natural Science Foundation of China (52372045, 22075081, 22279161, 22309144, and U1710252), National Key R&D Program of China (2021YFA1201503), Shanghai Sailing Program of China (23YF1408900), Natural Science Foundation of Jiangsu Province (BK. 20210130), China Postdoctoral Science Foundation (2023M731084, 2024M762318) as well as the Opening funding from Key Laboratory of Engineering Dielectrics and Its Application (Harbin University of Science and Technology) (No. KFM202507, Ministry of Education) are acknowledged. The author thanks the scientific support from Nano-X, Suzhou Institute of Nano-Tech and Nano-Bionics, Chinese Academy of Sciences.

Data availability

Data will be made available on request.

References

[1] H. Kim, J.C. Hyun, D.-H. Kim, J.H. Kwak, J.B. Lee, J.H. Moon, J. Choi, H.-D. Lim, S. J. Yang, H.M. Jin, D.J. Ahn, K. Kang, H.-J. Jin, H.-K. Lim, Y.S. Yun, Revisiting lithium- and sodium-ion storage in hard carbon anodes, Adv. Mater. 35 (2023) 2209128, https://doi.org/10.1002/adma.202209128.

[2] C. Qiu, A. Li, D. Qiu, Y. Wu, Z. Jiang, J. Zhang, J. Xiao, R. Yuan, Z. Jiang, X. Liu, X. Chen, H. Song, One-step construction of closed pores enabling high plateau capacity hard carbon anodes for sodium-ion batteries: closed-pore formation and energy storage mechanisms, ACS Nano 18 (2024) 11941–11954, https://doi.org/10.1021/acsnano.4c02046.

[3] K. Tian, H. He, X. Li, D. Wang, Z. Wang, R. Zheng, H. Sun, Y. Liu, Q. Wang, Boosting electrochemical reaction and suppressing phase transition with a high-entropy O_3-type layered oxide for sodium-ion batteries, J. Mater. Chem. A 10 (2022) 14943–14953, https://doi.org/10.1039/D2TA02451A.

[4] K.-H. Tian, C.-Q. Duan, Q. Ma, X.-L. Li, Z.-Y. Wang, H.-Y. Sun, S.-H. Luo, D. Wang, Y.-G. Liu, High-entropy chemistry stabilizing spinel oxide $(CoNiZnXMnLi)_3O_4$ (X = Fe, Cr) for high-performance anode of Li-ion batteries, Rare Met. 41 (2022) 1265–1275, https://doi.org/10.1007/s12598-021-01872-4.

[5] D. Chen, W. Zhang, K. Luo, Y. Song, Y. Zhong, Y. Liu, G. Wang, B. Zhong, Z. Wu, X. Guo, Hard carbon for sodium storage: mechanism and optimization strategies toward commercialization, Energ. Environ. Sci. 14 (2021) 2244–2262, https://doi.org/10.1039/D0EE03916K.

[6] X. Chen, C. Liu, Y. Fang, X. Ai, F. Zhong, H. Yang, Y. Cao, Understanding of the sodium storage mechanism in hard carbon anodes, Carbon Energy 4 (2022) 1133–1150, https://doi.org/10.1002/cey2.196.

[7] X. Fan, X. Kong, P. Zhang, J. Wang, Research progress on hard carbon materials in advanced sodium-ion batteries, Energy Storage Mater. 69 (2024) 103386, https://doi.org/10.1016/j.ensm.2024.103386.

[8] N. Sun, Z. Guan, Y. Liu, Y. Cao, Q. Zhu, H. Liu, Z. Wang, P. Zhang, B. Xu, Extended "adsorption–insertion" model: a new insight into the sodium storage mechanism of hard carbons, Adv. Energy Mater. 9 (2019) 1901351, https://doi.org/10.1002/aenm.201901351.

[9] H. Mao, S. Yang, Y. Yang, J. Yang, G. Yuan, M. Zheng, H. Hu, Y. Liang, X. Yu, Hybrid catalyst-assisted synthesis of multifunctional carbon derived from Camellia shell for high-performance sodium-ion batteries and sodium-ion hybrid capacitors, Carbon Neutralization 3 (2024) 673–688, https://doi.org/10.1002/cnl2.146.

[10] D. Qiu, W. Zhao, B. Zhang, M.T. Ahsan, Y. Wang, L. Zhang, X. Yang, Y. Hou, Ni-single atoms modification enabled kinetics enhanced and ultra-stable hard carbon anode for sodium-ion batteries, Adv. Energy Mater. 14 (2024) 2400002, https://doi.org/10.1002/aenm.202400002.

[11] Y. Chu, J. Zhang, Y. Zhang, Q. Li, Y. Jia, X. Dong, J. Xiao, Y. Tao, Q.-H. Yang, Reconfiguring hard carbons with emerging sodium-ion batteries: a perspective, Adv. Mater. 35 (2023) 2212186, https://doi.org/10.1002/adma.202212186.

[12] Z. Tang, R. Zhang, H. Wang, S. Zhou, Z. Pan, Y. Huang, D. Sun, Y. Tang, X. Ji, K. Amine, M. Shao, Revealing the closed pore formation of waste wood-derived hard carbon for advanced sodium-ion battery, Nat. Commun. 14 (2023) 6024, https://doi.org/10.1038/s41467-023-39637-5.

[13] Z. Hou, M. Jiang, D. Lei, X. Zhang, Y. Gao, J.-G. Wang, Regulation of pseudographitic carbon domain to boost sodium energy storage, Nano Res. 17 (2024) 5188–5196, https://doi.org/10.1007/s12274-024-6448-1.

[14] D. Qin, Z. Liu, Y. Zhao, G. Xu, F. Zhang, X. Zhang, A sustainable route from corn stalks to N, P-dual doping carbon sheets toward high performance sodium-ion batteries anode, Carbon 130 (2018) 664–671, https://doi.org/10.1016/j.carbon.2018.01.007.

[15] M. Li, J. Hu, L. Xu, G. Liu, Y. Sun, Y. Lei, X. Zhang, L. Zhang, X. Li, Multi-synergistic regulation of hard carbon via a green bioengineering strategy to achieve high-capacity sodium-ion storage, Green Chem. 27 (2025) 2696–2705, https://doi.org/10.1039/D4GC05497K.

[16] L. Yuan, Q. Zhang, Y. Pu, X. Qiu, C. Liu, H. Wu, Modulating intrinsic defect structure of fibrous hard carbon for super-fast and high-areal sodium energy storage, Adv. Energy Mater. 14 (2024) 2400125, https://doi.org/10.1002/aenm.202400125.

[17] Z. Heidarinejad, M.H. Dehghani, M. Heidari, G. Javedan, I. Ali, M. Sillanpää, Methods for preparation and activation of activated carbon: a review, Environ. Chem. Lett. 18 (2020) 393–415, https://doi.org/10.1007/s10311-019-00955-0.

[18] J. Meng, Z. Tong, H. Sun, Y. Liu, S. Zeng, J. Xu, Q. Xia, Q. Pan, S. Dou, H. Yu, Metal-free boron/phosphorus co-doped nanoporous carbon for highly efficient benzyl alcohol oxidation, Adv. Sci. 9 (2022) 2200518, https://doi.org/10.1002/advs.202200518.

[19] B. Chen, T. Wang, S. Zhao, J. Tan, N. Zhao, S.P. Jiang, Q. Zhang, G. Zhou, H.-M. Cheng, Efficient reversible conversion between MoS_2 and Mo/Na_2S enabled by graphene-supported single atom catalysts, Adv. Mater. 33 (2021) 2007090, https://doi.org/10.1002/adma.202007090.

[20] Z. Liang, J. Shen, X. Xu, F. Li, J. Liu, B. Yuan, Y. Yu, M. Zhu, Advances in the development of single-atom catalysts for high-energy-density lithium-sulfur batteries, Adv. Mater. 34 (2022) 2200102, https://doi.org/10.1002/adma.202200102.

[21] W. Xiao, X. Jiang, X. Liu, W. Zhou, Z.N. Garba, I. Lawan, L. Wang, Z. Yuan, Adsorption of organic dyes from wastewater by metal-doped porous carbon materials, J. Clean. Prod. 284 (2021) 124773, https://doi.org/10.1016/j.jclepro.2020.124773.

[22] J. Wang, J. Zhang, S. Cheng, J. Yang, Y. Xi, X. Hou, Q. Xiao, H. Lin, Long-life dendrite-free lithium metal electrode achieved by constructing a single metal atom anchored in a diffusion modulator layer, Nano Lett. 21 (2021) 3245–3253, https://doi.org/10.1021/acs.nanolett.1c00534.

[23] J. Wang, L. Jia, J. Zhong, Q. Xiao, C. Wang, K. Zang, H. Liu, H. Zheng, J. Luo, J. Yang, H. Fan, W. Duan, Y. Wu, H. Lin, Y. Zhang, Single-atom catalyst boosts electrochemical conversion reactions in batteries, Energy Storage Mater. 18 (2019) 246–252, https://doi.org/10.1016/j.ensm.2018.09.006.

[24] J. Wang, L. Jia, S. Duan, H. Liu, Q. Xiao, T. Li, H. Fan, K. Feng, J. Yang, Q. Wang, M. Liu, J. Zhong, W. Duan, H. Lin, Y. Zhang, Single atomic cobalt catalyst significantly accelerates lithium ion diffusion in high mass loading Li_2S cathode, Energy Storage Mater. 28 (2020) 375–382, https://doi.org/10.1016/j.ensm.2020.03.023.

[25] H.-Y. Zhuo, X. Zhang, J.-X. Liang, Q. Yu, H. Xiao, J. Li, Theoretical understandings of graphene-based metal single-atom catalysts: stability and catalytic performance, Chem. Rev. 120 (2020) 12315–12341, https://doi.org/10.1021/acs.chemrev.0c00818.

[26] L. Yang, X. Wang, X. Cheng, Y. Zhang, C. Ma, Y. Zhang, J. Wang, W. Qiao, L. Ling, Regulating Fe aggregation state via unique Fe-N-V pre-coordination to optimize the adsorption-catalysis effect in high-performance lithium-sulfur batteries, Adv. Funct. Mater. 33 (2023) 2303705, https://doi.org/10.1002/adfm.202303705.

[27] Y. Cui, Z. Cao, Y. Zhang, H. Chen, J. Gu, Z. Du, Y. Shi, B. Li, S. Yang, Single-atom sites on MXenes for energy conversion and storage, Small Sci. 1 (2021) 2100017, https://doi.org/10.1002/smsc.202100017.

[28] J. Wang, L. Li, H. Hu, H. Hu, Q. Guan, M. Huang, L. Jia, H. Adenusi, K.V. Tian, J. Zhang, S. Passerini, H. Lin, Toward dendrite-free metallic lithium anodes: from structural design to optimal electrochemical diffusion kinetics, ACS Nano 16 (2022) 17729–17760, https://doi.org/10.1021/acsnano.2c08480.

[29] J. Wang, J. Zhang, S. Duan, L. Jia, Q. Xiao, H. Liu, H. Hu, S. Cheng, Z. Zhang, L. Li, W. Duan, Y. Zhang, H. Lin, Lithium atom surface diffusion and delocalized deposition propelled by atomic metal catalyst toward ultrahigh-capacity dendrite-free lithium anode, Nano Lett. 22 (2022) 8008–8017, https://doi.org/10.1021/acs.nanolett.2c02611.

[30] Y. Lin, J. Wang, X. Zhang, X. Cheng, Q. Zhuang, J. Zhang, Q. Guan, Y. Wang, C. Shen, H. Lin, L. Zhan, L. Ling, Y. Zhang, Single atom-particle tandem catalysis enables enhanced desolvation kinetics for low-temperature Li-S batteries, Adv. Funct. Mater. (2025) 2501496, https://doi.org/10.1002/adfm.202501496.

[31] F. Na, X. Li, J. Wang, X. Cheng, J. Zhang, Y. Wang, H. Lin, L. Zhan, L. Ling, Y. Zhang, Immobilizing single atom on high-entropy oxides as separator regulators for catalyzing low-temperature lithium-sulfur battery, Energy Storage Mater. 78 (2025) 104228, https://doi.org/10.1016/j.ensm.2025.104228.

[32] G. Li, Y. Tang, Y. Wang, S. Cui, H. Chen, Y. Hu, H. Pang, L. Han, Single atomic Cu–C_3 sites catalyzed interfacial chemistry in Bi@C for ultra–stable and ultrafast sodium–ion batteries, Angew. Chem. Int. Ed. (2024) e202417602, https://doi.org/10.1002/anie.202417602.

[33] J. Wang, J. Zhang, J. Wu, M. Huang, L. Jia, L. Li, Y. Zhang, H. Hu, F. Liu, Q. Guan, M. Liu, H. Adenusi, H. Lin, S. Passerini, Interfacial “Single-atom-in-defects” catalysts accelerating Li^+ desolvation kinetics for long-lifespan lithium-metal batteries, Adv. Mater. 35 (2023) 2302828, https://doi.org/10.1002/adma.202302828.

[34] G. Liu, H. Yuan, Z. Wang, N. Qin, Y. Huang, Y. Cao, Y. Li, W. Lu, C. Zeng, Q. Liu, Z. Lu, Cu single atoms regulating nitrogen active-sites of g-C_3N_4 for sodium ion storage, Energy Storage Mater. 71 (2024) 103608, https://doi.org/10.1016/j.ensm.2024.103608.

[35] C. Lv, K. Huang, Y. Fan, J. Xu, C. Lian, H. Jiang, Y. Zhang, C. Ma, W. Qiao, J. Wang, L. Ling, Electrocatalytic reduction of carbon dioxide in confined microspace utilizing single nickel atom decorated nitrogen-doped carbon nanospheres, Nano Energy 111 (2023) 108384, https://doi.org/10.1016/j.nanoen.2023.108384.

[36] X. Jiao, J. Lei, Z. Huang, Y. Zuo, Z. Zhuang, Y. Luo, J. Qi, Z. Wang, L. Lu, W. Yan, J. Zhang, Axial coordination regulating electronic delocalization of p-block in N_4 sites to accelerate sulfur reduction reaction, Adv. Funct. Mater. (2025) 2505204, https://doi.org/10.1002/adfm.202505204.

[37] S. Yin, Y. Li, J. Yang, J. Liu, S. Yang, X. Cheng, H. Huang, R. Huang, C.-T. Wang, Y. Jiang, S. Sun, Unveiling low temperature assembly of dense Fe-N_4 active sites via hydrogenation in advanced oxygen reduction catalysts, Angew. Chem. Int. Ed. 63 (2024) e202404766, https://doi.org/10.1002/anie.202404766.

[38] Z. Cao, Y. Zhang, Y. Cui, J. Gu, Z. Du, Y. Shi, K. Shen, H. Chen, B. Li, S. Yang, Harnessing the unique features of 2D materials toward dendrite-free metal anodes, Energy Environ. Mater. 5 (2022) 45–67, https://doi.org/10.1002/eem2.12165.

[39] H. Chen, Z. Cao, J. Gu, Y. Cui, Y. Zhang, Z. Zhao, Z. Cheng, Q. Zhao, B. Li, S. Yang, Creating new battery configuration associated with the functions of primary and rechargeable lithium metal batteries, Adv. Energy Mater. 11 (2021) 2003746, https://doi.org/10.1002/aenm.202003746.

[40] Y. Zhou, F. Wei, H. Qi, Y. Chai, L. Cao, J. Lin, Q. Wan, X. Liu, Y. Xing, S. Lin, A. Wang, X. Wang, T. Zhang, Peripheral-nitrogen effects on the Ru1 centre for highly efficient propane dehydrogenation, Nat. Catal. 5 (2022) 1145–1156, https://doi.org/10.1038/s41929-022-00885-1.

[41] Y. Wang, Z. Yi, L. Xie, Y. Mao, W. Ji, Z. Liu, X. Wei, F. Su, C.-M. Chen, Releasing free radicals in precursor triggers the formation of closed pores in hard carbon for sodium-ion batteries, Adv. Mater. 36 (2024) 2401249, https://doi.org/10.1002/adma.202401249.

[42] J.C. Hyun, H.M. Jin, J.H. Kwak, S. Ha, D.H. Kang, H.S. Kim, S. Kim, M. Park, C. Y. Kim, J. Yoon, J.S. Park, J.-Y. Kim, H.-D. Lim, S.Y. Cho, H.-J. Jin, Y.S. Yun, Design guidelines for a high-performance hard carbon anode in sodium ion batteries, Energ. Environ. Sci. 17 (2024) 2856–2863, https://doi.org/10.1039/D4EE00315B.

[43] Z. Zhou, Z. Wang, L. Fan, In-situ capture defects through molecule grafting assisted in coal-based hard carbon anode for sodium-ion batteries, Chem. Eng. J. 490 (2024) 151428, https://doi.org/10.1016/j.cej.2024.151428.

[44] B. Zhao, X. Li, L. Shang, C. Qiu, R. Yuan, H. Liu, T. Liu, A. Li, X. Chen, H. Song, Regulating oxygen functionalities of cellulose-derived hard carbon toward superior sodium storage, J. Mater. Chem. A 12 (2024) 5834–5845, https://doi.org/10.1039/D3TA07775F.

[45] Y. Huang, X. Zhong, X. Hu, Y. Li, K. Wang, H. Tu, W. Deng, G. Zou, H. Hou, X. Ji, Rationally designing closed pore structure by carbon dots to evoke sodium storage sites of hard carbon in low-potential region, Adv. Funct. Mater. 34 (2023) 2308392, https://doi.org/10.1002/adfm.202308392.

[46] X. Yin, Z. Wang, Y. Liu, Z. Lu, H. Long, T. Liu, J. Zhang, Y. Zhao, Insight into the influence of ether and ester electrolytes on the sodium-ion transportation kinetics for hard carbon, Nano Res. 16 (2023) 10922–10930, https://doi.org/10.1007/s12274-023-5793-9.

[47] L. Wang, Z. Xu, P. Lin, Y. Zhong, X. Wang, Y. Yuan, J. Tu, Oxygen-crosslinker effect on the electrochemical characteristics of asphalt-based hard carbon anodes for sodium-ion batteries, Adv. Energy Mater. (2024) 2403084, https://doi.org/10.1002/aenm.202403084.

[48] Z. Tang, H. Wang, P.-F. Wu, S.-Y. Zhou, Y.-C. Huang, R. Zhang, D. Sun, Y.-G. Tang, H.-Y. Wang, Electrode–electrolyte interfacial chemistry modulation for ultra-high rate sodium-ion batteries, Angew. Chem. Int. Ed. 61 (2022) e202200475, https://doi.org/10.1002/anie.202200475.

[49] Y. He, D. Liu, J. Jiao, Y. Liu, S. He, Y. Zhang, Q. Cheng, Y. Fang, X. Mo, H. Pan, R. Wu, Pyridinic N-dominated hard carbon with accessible carbonyl groups enabling 98% initial coulombic efficiency for sodium-ion batteries, Adv. Funct. Mater. 34 (2024) 2403144, https://doi.org/10.1002/adfm.202403144.

[50] H. Qiang, M. Shi, F. Wang, M. Xia, Biomass-based N/P co-doped hierarchical porous carbon fabricated by a facile dual physico-chemical activation strategy for efficient capacitive deionization, Sep. Purif. Technol. 333 (2024) 125915, https://doi.org/10.1016/j.seppur.2023.125915.

[51] L. Yang, Y. Pan, Z. Zhou, Y. Zhang, J. Xu, C. Ma, Y. Zhang, J. Wang, W. Qiao, L. Ling, Vanadium as auxiliary for Fe–V dual-atom electrocatalyst in lithium–sulfur batteries: “3d in 2d” morphology inducer and coordination structure regulator, ACS Nano 17 (2023) 17405–17416, https://doi.org/10.1021/acsnano.3c05483.

[52] Z. Zheng, S. Hu, W. Yin, J. Peng, R. Wang, J. Jin, B. He, Y. Gong, H. Wang, H.J. Fan, CO_2-etching creates abundant closed pores in hard carbon for high-plateau-capacity sodium storage, Adv. Energy Mater. 14 (2024) 2303064, https://doi.org/10.1002/aenm.202303064.

[53] Z. Wu, Y. Zuo, Y. Zhang, X. Li, J. Zhang, Y. Wang, C. Shen, X. Cheng, M. Liu, H. Liu, H. Lin, J. Wang, L. Zhan, L. Ling, Modulating inner Helmholtz layer by electrocatalytically sieving $[Zn(H_2O)_6]^{2+}$ for 10000-cycle zinc-ion hybrid capacitors under extremely harsh conditions, Energy Storage Mater. 70 (2024) 103463, https://doi.org/10.1016/j.ensm.2024.103463.

[54] J. Gu, Y. Zhang, Y. Shi, Y. Jin, H. Chen, X. Sun, Y. Wang, L. Zhan, Z. Du, S. Yang, M. Li, Heteroatom immobilization engineering toward high-performance metal anodes, ACS Nano 18 (2024) 25966–25985, https://doi.org/10.1021/acsnano.4c08831.

[55] Q. Guan, J. Wang, Q. Zhuang, J. Zhang, L. Li, L. Jia, Y. Zhang, H. Hu, H. Hu, S. Cheng, H. Zhang, H. Li, M. Liu, S. Wang, H. Lin, Self-tandem catalysis of fast Mg^{2+} desolvation and sulfur conversions for ultrahigh-performance Mg–S batteries via serially-assembled atomic reactors, Energ. Environ. Sci. 17 (2024) 3765–3775, https://doi.org/10.1039/D3EE04028C.

[56] J. Wang, J. Zhang, Y. Zhang, H. Li, P. Chen, C. You, M. Liu, H. Lin, S. Passerini, Atom-level tandem catalysis in lithium metal batteries, Adv. Mater. 36 (2024) 2402792, https://doi.org/10.1002/adma.202402792.

[57] J. Dong, X. Cheng, H. Yang, H. Li, H. Liu, L. Jia, Y. Zhang, Q. Guan, J. Jia, F. Wu, J. Zhang, M. Liu, H. Lin, J. Wang, Suspension electrolytes with catalytically self-expediating desolvation kinetics for low-temperature zinc metal batteries, Adv. Mater. 37 (2025) 2501079, https://doi.org/10.1002/adma.202501079.

[58] Y. Zhang, H. Zhou, J. Gu, H. Yang, X. Cheng, J. Zhang, J. Wang, Y. Wang, H. Lin, J. Wang, L. Zhan, L. Ling, Homogeneous low-tortuosity membrane with fast ion transfer towards life-durable low-temperature zinc metal batteries, Energy Storage Mater. 76 (2025) 104161, https://doi.org/10.1016/j.ensm.2025.104161.

[59] L. Jia, H. Hu, X. Cheng, H. Dong, H. Li, Y. Zhang, H. Zhang, X. Zhao, C. Li, J. Zhang, H. Lin, J. Wang, Toward low-temperature zinc-ion batteries: strategy, progress, and prospect in vanadium-based cathodes, Adv. Energy Mater. 14 (2024) 2304010, https://doi.org/10.1002/aenm.202304010.

[60] X. Zhang, X. Li, Y. Zhang, X. Li, Q. Guan, J. Wang, Z. Zhuang, Q. Zhuang, X. Cheng, H. Liu, J. Zhang, C. Shen, H. Lin, Y. Wang, L. Zhan, L. Ling, Accelerated Li^+ desolvation for diffusion booster enabling low-temperature sulfur redox kinetics via electrocatalytic carbon-grazfted-CoP porous nanosheets, Adv. Funct. Mater. 33 (2023) 2302624, https://doi.org/10.1002/adfm.202302624.

[61] Y. Wang, H. Lan, S. Dong, Q. Zhu, L. Cheng, H. Wang, J. Wang, S. Wang, M. Tang, K.M. Shodievich, G. Wang, H. Wang, A high-power rechargeable sodium-ion full battery operating at 40 °C, Adv. Funct. Mater. 34 (2024) 2315498, https://doi.org/10.1002/adfm.202315498.

[62] X. Zhao, P. Shi, H. Wang, Q. Meng, X. Qi, G. Ai, F. Xie, X. Rong, Y. Xiong, Y. Lu, Y.-S. Hu, Unlocking plateau capacity with versatile precursor crosslinking for carbon anodes in Na-ion batteries, Energy Storage Mater. 70 (2024) 103543, https://doi.org/10.1016/j.ensm.2024.103543.

[63] X. Feng, Y. Li, Y. Li, M. Liu, L. Zheng, Y. Gong, R. Zhang, F. Wu, C. Wu, Y. Bai, Unlocking the local structure of hard carbon to grasp sodium-ion diffusion behavior for advanced sodium-ion batteries, Energ. Environ. Sci. 17 (2024) 1387–1396, https://doi.org/10.1039/D3EE03347C.

[64] M. Song, Z. Hu, C. Yuan, P. Dai, T. Zhang, L. Dong, T. Jin, C. Shen, K. Xie, Locally curved surface with CoN_4 sites enables hard carbon with superior sodium-ion storage performances at 40 °C, Adv. Energy Mater. 14 (2024) 2304537, https://doi.org/10.1002/aenm.202304537.

[65] S. Zhao, F. Huang, Weakly solvating few-layer-carbon interface toward high initial coulombic efficiency and cyclability hard carbon anodes, ACS Nano 18 (2024) 1733–1743, https://doi.org/10.1021/acsnano.3c11171.

[66] M. Liu, F. Wu, Y. Gong, Y. Li, Y. Li, X. Feng, Q. Li, C. Wu, Y. Bai, Interfacial-catalysis-enabled layered and inorganic-rich sei on hard carbon anodes in ester electrolytes for sodium-ion batteries, Adv. Mater. 35 (2023) 2300002, https://doi.org/10.1002/adma.202300002.

[67] Z. Lu, H. Yang, Y. Guo, H. Lin, P. Shan, S. Wu, P. He, Y. Yang, Q.-H. Yang, H. Zhou, Consummating ion desolvation in hard carbon anodes for reversible sodium storage, Nat. Commun. 15 (2024) 3497, https://doi.org/10.1038/s41467-024-47522-y.

[68] S.-Y. Jun, K. Shin, C.Y. Son, S. Kim, J. Park, H.-S. Kim, J.-Y. Hwang, W.-H. Ryu, Ultra-Long and rapid operating sodium metal batteries enabled by multifunctional polarizable interface stabilizer, Adv. Energy Mater. 14 (2024) 2304504, https://doi.org/10.1002/aenm.202304504.